

RESEARCH

Open Access



Neuroinflammation and hypoxia promote astrocyte phenotypic transformation and propel neurovascular dysfunction in brain arteriovenous malformation

Tianqi Tu^{1,2,6,7†}, Zhenghong Peng^{2,3†}, Lihan Zhang^{1,2†}, Jieru Yang^{1,2}, Kecheng Guo^{1,2}, Xiaogang Tang^{1,2}, Jiasen Ye^{1,2}, Fan Zhang^{1,2}, An Huang³, Jiaxing Yu⁵, Changren Huang^{1,2}, Hongqi Zhang⁵, Donghai Wang^{6,7,8*}, Jianhua Peng^{1,2*} and Yong Jiang^{1,2,3,4*}

Abstract

Brain arteriovenous malformation (BAVM) is a complex cerebrovascular disease characterized by an abnormal high-flow vascular network, which increases the risk of hemorrhage, particularly in young individuals. Endothelial dysfunction has traditionally been considered the primary cause, while the contributions of the microenvironment and glial cells have not been fully explored. Astrocytes, as a key component of the central nervous system, play a crucial role in regulating neurovascular function, maintaining the integrity of the blood–brain barrier, and ensuring neural homeostasis. However, under the pathological conditions of BAVM, the phenotypic changes in astrocytes and their role in disease progression remain poorly understood. In our study, we emphasized the critical role of neuroinflammation and hypoxia in the progression of BAVM within its pathological microenvironment. Specifically, reactive astrocytes undergo phenotypic changes under these pathological conditions, significantly promoting vascular instability. Moreover, nitric oxide (NO) produced by BAVM endothelial cells activates signaling pathways that stabilize HIF-1 α in astrocytes, initiating a “hypoxic” gene program under normoxic conditions. Furthermore, we discovered that COX-2, a direct target gene of HIF-1 α , is upregulated in the BAVM microenvironment. These changes promoted endothelial dysfunction and vascular fragility, creating a vicious cycle that exacerbates hemorrhage risk. The application of COX-2 inhibitors significantly reduced neuroinflammation, stabilized blood vessels, and decreased hemorrhage risk. Our findings highlighted the crucial interaction between the BAVM microenvironment and astrocytes in driving disease progression, suggesting that COX-2 could be a potential therapeutic target for stabilizing BAVM vessels and reducing hemorrhagic events.

Keywords Brain arteriovenous malformation, Astrocytes, Neuroinflammation, Hypoxia, Cyclooxygenase-2

[†]Tianqi Tu, Zhenghong Peng and Lihan Zhang contributed equally and are recognized as co-first authors.

*Correspondence:

Donghai Wang
drwangdonghai@sdu.edu.cn
Jianhua Peng
pengjianhua@swmu.edu.cn
Yong Jiang
jiangyong@swmu.edu.cn

Full list of author information is available at the end of the article



Introduction

Brain arteriovenous malformation (BAVM) is a complex cerebrovascular disease characterized by an abnormal high-flow vascular network [1]. Due to the tendency to leak or rupture, these vascular malformations are a leading cause of hemorrhagic stroke, particularly in young individuals [2]. Current treatment options are limited to endovascular embolization, surgical resection, or stereotactic radiosurgery, which carry significant risks and may not always be feasible depending on the location of the malformation [3, 4]. Therefore, further investigation into the factors affecting BAVM stability and rupture hemorrhage is crucial, as it may provide a basis for the development of pharmacological strategies aimed at reducing hemorrhage risk. The characteristic pathological microenvironment of BAVM includes significant neuroinflammation and hypoxia, which are closely associated with disease progression and play key roles in increasing the risk of hemorrhage and rebleeding [5, 6]. However, specific cellular response mechanisms within the BAVM microenvironment remain poorly understood.

Astrocytes are key components of the neurovascular unit, playing a critical role in maintaining homeostasis within the central nervous system (CNS) [7, 8]. In response to various injuries and disease states, astrocytes undergo phenotypic transformations, accompanied by significant changes in cellular morphology, function, and gene expression [9–11]. Studies have shown that reactive astrogliosis increases VEGF secretion, thereby accelerating the progression of CNS diseases [11, 12]. Moreover, these “neuroinflammatory astrocytes” not only intensify local inflammatory responses but may also compromise endothelial stability, promoting vascular remodeling and raising the risk of hemorrhage [13, 14]. Intriguingly, the pathological environment in BAVM may induce phenotypic shifts in astrocytes. However, the mechanisms by which astrocytes contribute to BAVM pathology, including how the pathological environment induces phenotypic changes that alter their interactions with blood vessels, remain unclear and require further investigation.

Cyclooxygenase-2 (COX-2), an enzyme highly expressed under inflammatory conditions, is considered a key regulatory factor that promotes the production of inflammatory mediators such as prostaglandins, thereby activating the inflammatory response and vascular remodeling [15–17]. Abnormal expression of COX-2 has also been observed in other vascular malformation diseases, such as brain aneurysms and cavernous malformations, and is thought to potentially affect endothelial stability and disease progression [13, 18, 19]. Therefore, therapeutic attempts targeting COX-2 may

offer dual benefits: on one hand, they could help alleviate neuroinflammation, reducing secondary damage caused by the pathological microenvironment, and on the other, they may reduce vascular instability, lowering the risk of hemorrhage. These characteristics enhance its potential effectiveness in the treatment of BAVM disease.

In our previous study, we revealed the high prevalence of *KRAS/BRAF* somatic mutations in brain and spinal cord arteriovenous malformations [20]. Building upon this, we innovatively established a BAVM mouse model that simulates the genetic background and pathophysiological characteristics of sporadic human BAVM [21]. In this study, to further investigate the pathological microenvironment of BAVM, we utilize a newly established animal model of BAVM with a hemorrhagic phenotype to uncover how astrocytes with distinct phenotypes within the BAVM pathological microenvironment drive disease progression and compromise neurovascular integrity. Additionally, it seeks to identify novel therapeutic strategies to stabilize fragile vessels and mitigate the risk of hemorrhagic events.

Materials and methods

Animals

For this study, equal numbers of adult male and female C57BL/6 J mice, aged 6 weeks and weighing 18–22 g, were obtained from Chengdu Dashuo Laboratory Animal Co., Ltd. In our experiments, we utilized blinding and randomization methods to minimize bias in group allocation. Additionally, we ensured that the sample sizes were equal across groups, with a balanced representation of male and female mice in each group. All mice were housed in a controlled environment with a 12-h light/dark cycle, maintained at a temperature of 25 °C, and had free access to food and water. All animal procedures received approval from the Animal Ethics Committee of Southwest Medical University and were conducted in compliance with the National Institutes of Health guidelines for the Care and Use of Laboratory Animals.

Adeno-associated virus injection

We obtained AAV-BR1-CAG-*Braf*^{V600E}-WPRESV40pA (abbreviated as AAV-BR1-*Braf*^{V600E}), AAV-BR1-EGFP and AAV-BR1 was obtained from Guangzhou PackGene Biotechnology Co., Ltd (Guangzhou, China) [21]. Firstly, 6-week-old male or female mice were administered 100 µl of phosphate-buffered saline (PBS) containing 2 × 10¹⁰ genome copies/mouse of AAV-BR1-EGFP by retro-orbital venous sinus injection. Fresh samples, including the brain, cerebellum, and spinal cord, were harvested four weeks after injection to verify expression levels and labeling efficiency. In the subsequent formal experiments,

we selected AAV-BR1-*Braf*^{V600E} or AAV-BR1 (control) and performed injections following the same strategy. This approach reduces fluorescence channel usage, accommodating multicolor fluorescence experiments.

Latex perfusion and clearing

The blue latex perfusion was performed based on our previous work [21]. First, blue latex was injected into the left ventricle, and specimens were fixed in 10% formalin for 24 h. Then the tissues were dehydrated in a methanol gradient (50%, 75%, 90%, and 100% for 24 h each). Subsequently, a 1:1 mixture of benzyl benzoate and benzyl alcohol was used to clear the tissues. The images were then captured using a stereomicroscope.

H&E staining

Consistent with our previous work, the euthanized mice were first perfused with a PBS solution (pH = 7.4) to clear the vasculature, followed by fixation of the brain tissue in a 4% (w/v) paraformaldehyde (PFA) solution for 24 h [21]. After fixation, the brain tissue was carefully extracted, embedded in paraffin, and sectioned into 5–10 μm thick slices using a microtome. The tissue sections were then subjected to hematoxylin and eosin (H&E) staining to examine general histological features.

Immunofluorescence staining and TUNEL staining

The brain tissue was perfused with PBS and fixed in 4% paraformaldehyde. After fixation, the tissue was dehydrated through a sucrose gradient (20% and 30% for 12 h each) and sliced into 10–40 μm thick coronal sections using a Leica cryostat. The tissue sections were allowed to warm to room temperature for 30 min, then incubated in antigen retrieval solution for 10 min. Following permeabilization with 0.5% Triton X-100 for 10 min, the sections were blocked with 5% goat serum for 1 h in room temperature (25 °C). Finally, the tissue sections were incubated overnight at 4 °C with the following primary antibodies: CD31 (1:50, BD Biosciences, 550274), eNOS (1:100, Thermo Fisher, PA1037), GFAP (1:400, Proteintech, 60190-1-AP), OCCLUDIN (1:500, Abcam, ab216327) and CLAUDIN-5 (1:500, Thermo Fisher, PA5-99,415). After being washed with PBS on the second day, the sections were incubated with the secondary antibody for 1 h in room temperature (25 °C). The secondary antibodies used were as follows: Alexa FluorTM 488 (1:400; ThermoFisher, #A-11006), Alexa FluorTM 546 (1:400; ThermoFisher, #A-11035) and Alexa FluorTM 647 (1:200; ThermoFisher, #A-21247 and #A-31573). Then the sections were mounted using an anti-fade mounting medium containing DAPI (Solarbio, S2110).

Confocal microscopy was used to acquire images with Z-axis information, with a step size of 2 μm , 10 layers, and a total scanning depth of 20 μm . The imaging parameters were as follows: Alexa Fluor 488 (488 nm laser line, excitation at 493 nm, emission at 517 nm, detection range 450–585 nm), Alexa Fluor 546 (556 nm laser line, excitation at 556 nm, emission at 573 nm, detection range 570–620 nm), Alexa Fluor 647 (640 nm laser line, excitation at 650 nm, emission at 665 nm, detection range 650–700) and DAPI (405 nm laser line, excitation at 353 nm, emission at 465 nm, detection range 400–580 nm). During imaging, the selected fields of view are matched between the Control and BAVM groups of mice. Data quantification and image rendering were performed using Imaris software (9.0.1 version). The parameters for surface generation in each group needed to be consistent, and the detailed procedures can be found in previous studies [22–24].

TUNEL staining of brain tissue was performed according to the instructions of the kit (Vazyme, China). After permeabilization of the brain tissue slices, the samples were equilibrated with 1X equilibration buffer for 20 min at room temperature (25 °C). Then, each slice was stained with 50 μL of TdT buffer in an incubator at 37 °C for 1 h. Next, immunofluorescence staining was performed as described above.

Primary astrocyte and endothelial cell extraction and culture

Primary astrocyte and endothelial cell extraction, as well as co-culture, were performed according to previously published protocols [13, 25]. The specific procedures are briefly outlined as follows:

Primary astrocyte extraction and culture

Cortical tissue was isolated from C57BL/6 J mice and placed in ice-cold PBS to remove blood. The tissue was minced and dissociated using DMEM/F12 medium containing 25 mM glucose and 10% FBS. The cell suspension was seeded in uncoated culture dishes at a density of 6×10^5 cells/cm² and cultured in a 37 °C, 5% CO₂ incubator for 7–10 days. During culture, the medium was changed every 3–4 days, and non-astrocytic cells were removed by mechanical scraping. The astrocytes were purified by selective attachment, resulting in cultures with >95% astrocyte purity. The cells were maintained in DMEM/F12 supplemented with 10% FBS and 1% penicillin–streptomycin.

Primary brain microvascular endothelial cell extraction and culture

Brain microvessels were isolated from the brains of C57BL/6 J mice, washed with ice-cold PBS, and

enzymatically digested with collagenase (Type IV, 1–2 mg/mL) and DNase I (50–100 µg/mL) for 30 min at 37 °C. After digestion, the cell suspension was filtered through a 70 µm cell strainer to remove undigested tissue. Endothelial cells were isolated by density gradient centrifugation using Ficoll, followed by plating in endothelial cell medium (ECM) containing 10% FBS and 1% penicillin–streptomycin. Cells were cultured at 37 °C in a 5% CO₂ incubator.

Co-culture was performed using Transwell, as described in previous studies [13, 25]. The upper chamber contained astrocytes, which were derived from untreated C57BL/6 J mice, while the lower chamber contained endothelial cells, derived from mice in the Control group and BAVM group, respectively.

Culture of mouse brain microvascular endothelial cells

To investigate the effect of astrocytes on endothelial cells, we replaced the medium of astrocytes induced by primary endothelial cells (in the previous steps) and cultured them separately for 12 h. The conditioned medium from astrocytes (from both the control-EC group and the BAVM-EC-induced group) was then collected and used to culture mouse brain microvascular endothelial cells Bend.3 (McellBank, China). After 24 h, cell samples were prepared for subsequent experiments.

Isolation of astrocytes from the brain

As described in our previous work [12], mice were anesthetized with pentobarbital sodium and sacrificed for brain extraction. To minimize the impact of spatial heterogeneity, we excluded the olfactory bulb, cerebellum, and medulla during sample collection and limited our analysis to brain regions. Using the high-activity brain enzyme digestion kit (DHABE-5003, RWD, China) and single-cell suspension preparation instrument (DSC-400, RWD, China), brain tissue was processed into a single-cell suspension. Myelin and red blood cells were removed with Myelin Removal Beads II (Miltenyi Biotec, Germany) and Red Blood Cell Lysis Buffer (Solarbio, China). The cell pellets were magnetically labeled with FcR Blocking reagent and Anti-ACSA-2 MicroBeads, following the manufacturer's guidelines. Isolated astrocytes were used for WB, RT-qPCR and RNA-seq analysis.

Western blot

Immunoblot analysis was conducted following the standard procedure outlined previously [21, 26]. Briefly, fresh brain tissue samples and primary astrocytes from each group were collected and prepared. Whole-cell lysates were prepared by homogenizing the samples in RIPA buffer (89901, Thermo Fisher Scientific) to

ensure efficient cell membrane disruption and protein extraction. The protein concentration in the lysates was subsequently measured using a BCA Protein Assay kit (P0012, Beyotime), which provides a sensitive and accurate method for quantifying total protein content. For western blot analysis, 20 µg of total protein was loaded. The antibodies used in this study included: eNOS (1:100, Thermo Fisher, PA1037), Cox2 (1:100, CST, #12282), HIF-1α (1:100, Novus, NB100-479), β-actin (1:1000, CST, #4967) and Anti-rabbit IgG, Antibody (1:1000, CST, #7074).

RNA isolation and RT-qPCR

Following the manufacturer's protocol, Total RNA isolated astrocytes and tissues was extracted utilizing the RNA isolater Total RNA Extraction Reagent (Vazyme, China). RNA concentration in each sample was determined using a NanoDrop 2000 spectrophotometer (Thermo Fisher Scientific, USA). cDNA was synthesized via reverse transcription with HiScript[®]III RT SuperMix for qPCR and gDNA wiper (Vazyme, China). RT-qPCR was performed on the Jena qTOWER real-time PCR system (Jena, Germany) with ChamQ[™] Universal SYBR[®] qPCR Master Mix (Vazyme, China). mRNA expression was normalized to β-actin, and relative expression was quantified using the 2^{-ΔΔCt} method.

Library construction and RNA sequencing

We followed the instructions (TD501-TD503, Vazyme, China) to construct the library from RNA extracted from primary astrocytes. Briefly, total RNA was extracted using the Trizol reagent (Vazyme) and RNeasy mini kit according to the manufacturers' instructions. After digesting the DNA in the sample with DNase, mRNA was enriched using magnetic beads with Oligo (dT). An interruption reagent was added to fragment the mRNA into short pieces. Six-base random primers were used to synthesize the first-strand complementary DNA (cDNA). Then, the reaction system for second-strand synthesis was prepared to generate the second-strand cDNA. End repair was performed, an A tail was added, sequencing adapters were ligated, the fragment size was selected, and PCR amplification was conducted. The constructed library was then sequenced using the Illumina Novaseq 6000 to generate 150 bp paired-end data. The RNA-seq sequencing were completed with the assistance of Shanghai Scientific Services Co, LTD.

Differential analysis and enrichment analysis

DEGs were evaluated using DESeq2 (version 1.34.0) package in R (version 4.2.0), using *p* adjust < 0.05 and |log₂FC| > 4 as cutoffs to define the DEGs. Kyoto Encyclopedia of Genes and Genomes (KEGG) is an

encyclopedia for understanding biological functions and related genetic or genomic information. To explore the main functions and roles of these differential genes, the clusterProfiler (version 4.0.5) Bioconductor packages were used to enrich gene ontologies (GO) and the Kyoto Encyclopedia of Genes and Genomes (KEGG), and the pathways with FDR < 0.05 were considered significant.

Treatment with celecoxib

For the Celecoxib treatment, male and female mice from both the control (AAV-BR1) and BAVM (AAV-BR1-*Braf*^{N600E}) groups were randomly assigned to one of two treatment conditions: Celecoxib (40 mg/kg, Celebrex) or vehicle (0.5% methylcellulose plus 0.025% Tween 20) [13]. Six-week-old mice (P42) were injected with AAV, and Celecoxib or vehicle was administered daily by oral gavage from P49 to P63, and then weekly from P63 to P70 ('P' stands for postnatal day). Both control and BAVM groups, including male and female mice, received the respective treatments. The animals were sacrificed at P80 for subsequent analysis. In this study, we employed a double-blind design. Mice were randomly assigned to experimental and control groups using a random number generator, and group allocations were coded. Both the experimenters conducting the interventions and those analyzing the data were blinded to the group assignments. Additionally, each group contained an equal number of male and female mice, ensuring the rigor of the randomization process, minimizing bias, and maintaining objectivity.

Behavioral testing

The behavioral scoring criteria for mice used in this study were based on previous work, and all behavioral tests were conducted by two independent experimenters who were blinded to the group allocation and interventions throughout the process. This approach was implemented to minimize potential bias and ensure the objectivity and reliability of the results [12, 21, 27].

Beam balance test

To evaluate balance and motor skills in mice, a Beam Balance test was conducted. Mice were assessed based on their ability to remain on and walk along a wooden beam for a 1-min period. Scoring criteria were as follows: inability to walk and fall (0); inability to walk but remain on the beam (1); walking with a fall (2); walking less than 20 cm (3); and walking beyond 20 cm (4).

The Rotarod test

The Rotarod test was employed to measure motor coordination, balance, and resistance to fatigue. In each trial, mice were placed on a horizontal rotating rod with

a diameter of 4.5 cm, which rotated at 4 rpm. Mice were permitted to run for a maximum duration of 5 min. Up to three trials were performed daily.

The wire test

Mice were evaluated using a wire hanging test, in which they were placed on a 2-mm diameter wire suspended 30 cm above a cushioned bedding surface. The test duration was 3 min, during which mice were permitted to hang or until a fall occurred. If a mouse fell, it was returned to the wire, with up to five repositioning attempts allowed within the 3-min assessment window.

The Morris water maze test

The Morris water maze test was employed to evaluate spatial learning and memory in BAVM mice. Testing was conducted in a large circular pool with opaque water maintained at 25 ± 2 °C. The pool was divided into four quadrants, with a transparent escape platform (10 cm in diameter) placed 1 cm below the water's surface in one quadrant. Over five training days, mice were introduced at one of four randomized starting points and given 60 s to locate the platform. Mice that failed to find it within the allotted time were gently guided to the platform by the experimenter and allowed a 10-s rest. On the sixth day, the platform was removed to test memory recall, while all other procedures were maintained. The frequency of entries into the target area was recorded.

The open field test

The open field test was employed to assess spontaneous locomotor activity in BAVM mouse models for the first time. Prior to the test, mice were acclimated in a quiet, well-lit environment. Each mouse was then individually placed in an open-field arena (50 × 50 × 25 cm) and allowed to explore freely. The total recording duration for each mouse was no less than 7 min. Locomotor activity was recorded and analyzed using Smart 3.0 software (Panlab, Spain), with a specific focus on the distance traveled during the final 4 min, providing a measure of their spontaneous movement and overall motor function. To ensure consistency and standardization in data analysis, we uniformly selected a 4-min time window from 2 min 30 s to 6 min 30 s after the start of the recording.

Data analysis and statistics

Statistical analysis was performed using GraphPad Prism Software (Version 8.4.0, GraphPad, La Jolla, CA). All continuous variables were presented as mean ± SD. Shapiro–Wilk normality test was performed to determine data distribution. For normally distributed data, two-tailed unpaired Student's t test for two groups

was applied, and one-way ANOVA followed by Tukey's multiple comparison test was used for multi-group comparisons. Kaplan–Meier plot was performed to analyze the survival rate and followed by Log-rank test to determine the difference in survival rate between groups. Two-sided $P < 0.05$ was considered statistically significant and are denoted as follows: * $P < 0.05$; ** $P < 0.01$; *** $P < 0.001$.

Results

Brain endothelial specific *Braf*^{V600E} overexpression induces BAVMs

In this study, we used an adeno-associated virus (AAV) with the BR1 serotype, which specifically targets endothelial cells in the CNS, to achieve the expression of the *Braf* mutation in CNS endothelial cells. To assess the expression efficiency and specificity, we first validated the system using AAV-BR1-CAG-eGFP-WPRE-SV40pA (AAV-BR1-EGFP). Six-week-old adult mice (P42) were selected and AAV-BR1-EGFP was injected via the orbital vein (as the Additional file 1: Fig. S1 A illustrated). Four weeks later, fresh brain and spinal cord tissues were collected and co-stained with CD31 to evaluate labeling efficiency and specificity (Additional file 1: Fig. S1 A). As shown in Additional file 1: Fig. S1B–D, this method successfully labeled blood vessels in the brain, cerebellum, and spinal cord, achieving nearly 90% vascular labeling efficiency with extremely high specificity.

Subsequently, we conducted follow-up experiments using AAV-BR1 and AAV-BR1-*Braf*^{V600E} to establish both the control group and the BAVM model (Considering that subsequent experiments involved multi-color fluorescence co-observation, we did not include fluorescent proteins in the AAV constructs). Similarly, 6-week-old mice (P42) were injected with AAV and sacrificed at four weeks post-injection for analysis (as the Fig. 1A illustrated). Observation of the collected brain tissues under a stereomicroscope revealed multifocal hemorrhages on the surfaces of the olfactory bulb, cerebrum, cerebellum, and medulla in the BAVM group, whereas no hemorrhages were detected in the control group (Fig. 1B–F). To confirm the formation of BAVM, we performed blue latex perfusion and collected tissues followed by whole brain clearing. The results clearly revealed typical BAVM lesions, characterized by dilated blood vessels accompanied by hemorrhage (Fig. 1G). H&E staining confirmed the presence of hemorrhage and thrombus formation surrounding the BAVM lesions (Fig. 1H). Additionally, Evans Blue Dye (EBD) perfusion revealed extensive leakage and hemorrhagic tendencies in BAVM lesions, underscoring the compromised vascular integrity (Fig. 1I). Immunostaining for CLAUDIN-5 and OCCLUDIN indicated a significant reduction in tight junction

protein coverage within these lesion vessels, indicating disrupted endothelial barrier function (Fig. 2A–D). These results explained the pronounced propensity of BAVM for leakage or rupture-induced hemorrhage, attributing it to the structural fragility of the vascular walls in typical BAVM lesions.

We also recorded the long-term survival of BAVM mice. In the AAV intervention group, six-week-old adult mice (P42) were injected with AAV at day 42, and then monitored for 20 weeks (140 days) after the initial injection (Additional file 2: Fig. S2 A, B). After 140 days of AAV injection, we observed scattered hemorrhagic lesions, which resembled the phenotype of another *Kras*-induced mouse model reported previously (Additional file 2: Fig. S2 C) [27]. All together, these results suggested that our new modeling strategy successfully established the BAVM model, which is characterized by focal hemorrhages.

Hypoxia, oxidative stress, and neuroinflammation are characteristic features of the pathological microenvironment in BAVM

Our previous work has confirmed the presence of a strong neuroinflammatory response in the BAVM microenvironment [21]. In this study, it was similarly revealed that this new preclinical model's pathological microenvironment is characterized by heightened neuroinflammatory responses, with markers such as *Mmp-9*, *Tnf- α* , *Il-6*, and *Il-1 β* showing significant elevation, indicative of active inflammatory signaling. (Fig. 2E–H). Previous research has demonstrated that endothelial nitric oxide synthase (eNOS) may contribute to VEGF-induced angiogenesis and increased vascular permeability, possibly by stabilizing hypoxia-inducible factor-1 α (HIF1- α) through nitric oxide (NO) production [28–31]. Our results revealed higher *Nos3* mRNA levels detected in BAVM brain tissues (Fig. 2I). To further investigate eNOS distribution and expression in BAVM lesions, we performed co-staining of eNOS and CD31 on brain tissue sections. As depicted in Fig. 2J, eNOS was predominantly localized within endothelial cells, with substantial accumulation observed in the endothelial cells of BAVM lesions. Western blot analysis further confirmed that eNOS protein levels were significantly elevated in BAVM tissues compared to controls (Fig. 2K, L). Similarly, compared to the control group, COX-2 was significantly increased at both the protein and mRNA levels in the BAVM brain tissue, reinforcing the notion of enhanced oxidative stress and inflammatory responses (Fig. 2K, M, N).

Collectively, these findings reveal a potential pathological vicious cycle: the loss of vascular stability in the BAVM microenvironment compromises

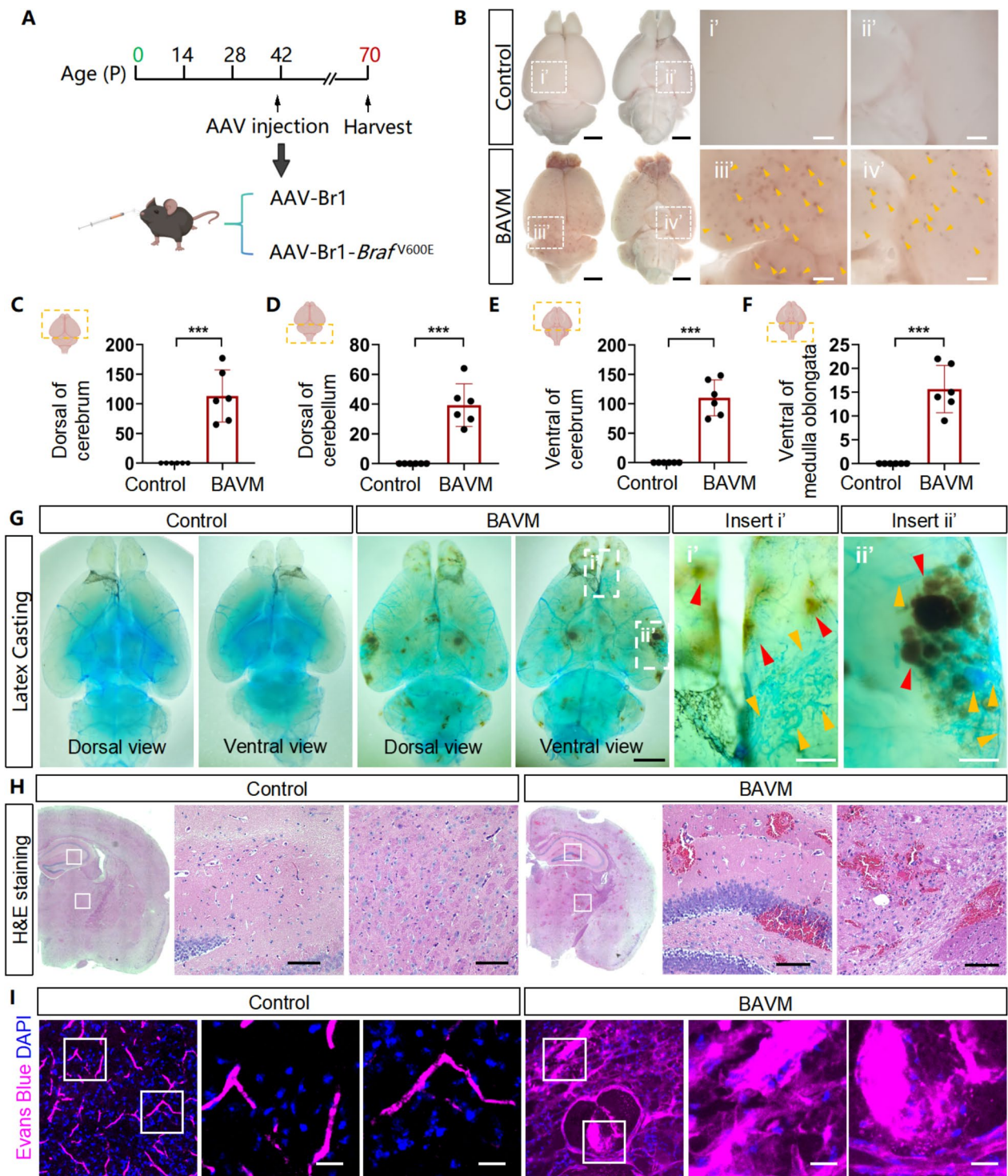


Fig. 1 Activation of *Brav*^{V600E} mutation drives BAVMs in mice, accompanied by an inflammatory and hypoxic microenvironment. **A** A diagram illustrating the model establishment. **B** Images of fresh brain tissues of control and BAVM group. Images of (i')–(iv') were locally magnified images. Yellow arrows indicate hemorrhagic spots. Black scale bar = 2 mm, white scale bar = 500 μ m. **C–F** The quantification of the number of surface hemorrhage (n = 6 mice). **G** Representative images of latex-casted clarified brains at 4th week after AAV injection. Images of (i')–(ii') were locally magnified images. Yellow arrows indicate the lesions and red arrows indicate hemorrhagic spots. Black scale bar = 2 mm and white Scale bar = 500 μ m. **H** Images of H&E staining of brain sections. Scale bar = 100 μ m. **I** Representative images of Evans Blue Dye perfusion in control and BAVM mice. Scale bar = 20 μ m

vessel integrity, predisposing lesions to rupture or extravasation, which exacerbates local hypoxia, oxidative stress, and inflammation. This progressive deterioration further weakens the vascular structure, perpetuating a cycle that escalates the risk of recurrent hemorrhage.

The unique phenotype of astrocytes in the BAVM pathological microenvironment may drive disease progression

BAVM has been studied as an endothelial cell-autonomous disease, with genetic mutations in endothelial cells serving as the genetic background [20, 32]. Although BAVM is a disease that impacts the neurovascular unit, our understanding of whether astrocytes contribute to its onset, progression, and the underlying mechanisms remains limited. This prompted us to investigate the relationship between astrocytes and the disease process in our murine models of BAVM. To understand the phenotypic changes of astrocytes, GFAP and CD31 dual immunofluorescence staining was performed. In the WT group, astrocytes displayed a typical resting, branched structure, with endfeet closely contacting the vascular walls, providing extensive vascular coverage, and supporting normal astrocyte-vascular interactions (Fig. 3A). However, around the BAVM lesions, astrocytes exhibited a significant phenotypic change, characterized by a distinct bundle-like morphology and a marked reduction in branching (Fig. 3A–C). It is well known that astrocytic end-feet play a crucial role in supporting the cerebral vascular barrier, regulating vascular permeability and facilitating neurovascular coupling [33–35]. To observe the coverage of astrocytic end-feet with specific phenotypes in the pathological microenvironment of BAVM, we performed double staining with AQP4 and CD31, and scanned three-dimensional structural images (including the Z-axis) under a high-magnification confocal microscope. In Fig. 3D, we can clearly see that astrocytic end-feet in the control group envelop the blood vessels. However, in the BAVM lesions, the coverage of end-feet was significantly reduced around dilated lumens (Fig. 3D).

Next, to further examine the role of astrocytes, we extracted primary astrocytes from the brain tissues of control and BAVM group mice following the methods used in our previous work (Fig. 3E) [12]. The WB (samples of isolated astrocytes) results showed that the expression level of HIF-1 α in the BAVM group was significantly higher than that in the control group (Fig. 3F, G). Next, the RT-qPCR results indicated that HIF-1 α targeted genes, including *Cd44*, *Angptl4* and *Loxl2* were significantly elevated in astrocytes from the BAVM group (Fig. 3H–J). These genes are associated with extracellular matrix (ECM) remodeling, cell migration, angiogenesis, and tissue repair [36]. In addition, we also observed a significant induction of HIF-1 α -regulated inflammatory genes, including cyclooxygenase-2 (*Cox2*) and monocyte chemoattractant protein-1 (*Mcp1*) (Fig. 3K, L). Previous studies have shown that astrocytes are a major source of VEGF-A, and that its expression is regulated by HIF-1 α [13, 14]. In our study, we also confirmed that the expression of *Vegf-a* in astrocytes within the BAVM microenvironment was significantly higher compared to the control group (Fig. 3M).

In line with this, through primary cell extraction and co-culture experiments, we also confirmed the phenotypic transformation of astrocytes, including the upregulation of HIF-1 α expression, as well as the transcriptional upregulation of *Cox-2* and *Vegf-a* (Additional file 3: Fig. S3 A–F). Although the in vitro co-culture induction method does not fully replicate the pathological microenvironment of BAVM, since endothelial cells are the source of the lesion, it still provides valuable insights into the underlying mechanisms. To further investigate the impact of reactive astrocytes on endothelial function, we co-cultured endothelial cells with astrocyte-conditioned medium (Additional file 4: Fig. S4 A). The results indicated that, under the influence of reactive astrocytes, the expression of *Icam-1* and *Vcam-1* in endothelial cells was increased, suggesting an inflammatory endothelial injury (Additional file 4: Fig. S4B, C). At the same time, the levels of tight junction proteins OCCLUDIN and ZO-1 decreased (Additional file 4: Fig. S4D–G). Additionally,

(See figure on next page.)

Fig. 2 Hypoxic, oxidative, and inflammatory microenvironment in BAVM formation. **A** Representative fluorescence images of immunostaining with CD31 and OCCLUDIN (OCLN) for each group. Scale bar = 20 μ m. The asterisk (*) represents the vascular lumen of BAVM. **B** The quantification of the ratio of OCLN + vessels/CD31 + vessels (%) (n = 3 mice). **C** Representative fluorescence images of immunostaining with CD31 and CLAUDIN-5 (CLDN5) for each group. Scale bar = 20 μ m. The asterisk (*) represents the vascular lumen of BAVM. **D** The quantification of the ratio of CLDN5 + vessels/CD31 + vessels (%) (n = 3 mice). **E–I** Relative mRNA levels of *Mmp-9*, *Tnf- α* , *Il-1 β* , *Il-6* and *Nos3* in control and BAVM mice (n = 5 mice). **J** Representative fluorescence images of immunostaining with CD31 and eNOS. Scale bar = 20 μ m. The asterisk (*) represents the vascular lumen of BAVM. **K** Representative Western blot images of eNOS and COX-2 in brain tissue from control group and BAVM mice. **L** The quantification of eNOS/ β -actin (n = 4 mice). **M** The quantification of COX-2/ β -actin (n = 4 mice). **N** Relative mRNA levels of *Cox-2* in control and BAVM mice (n = 5 mice)

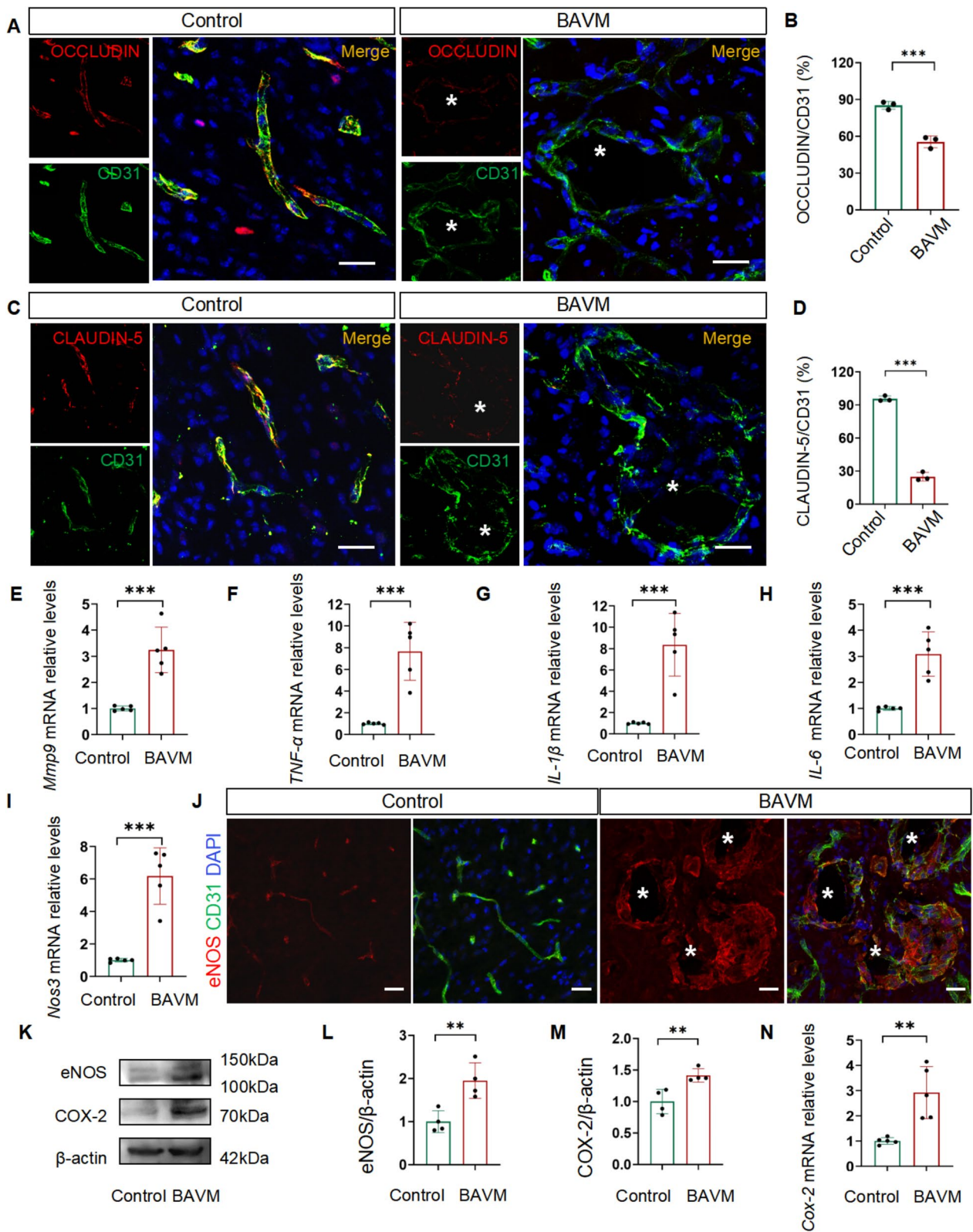


Fig. 2 (See legend on previous page.)

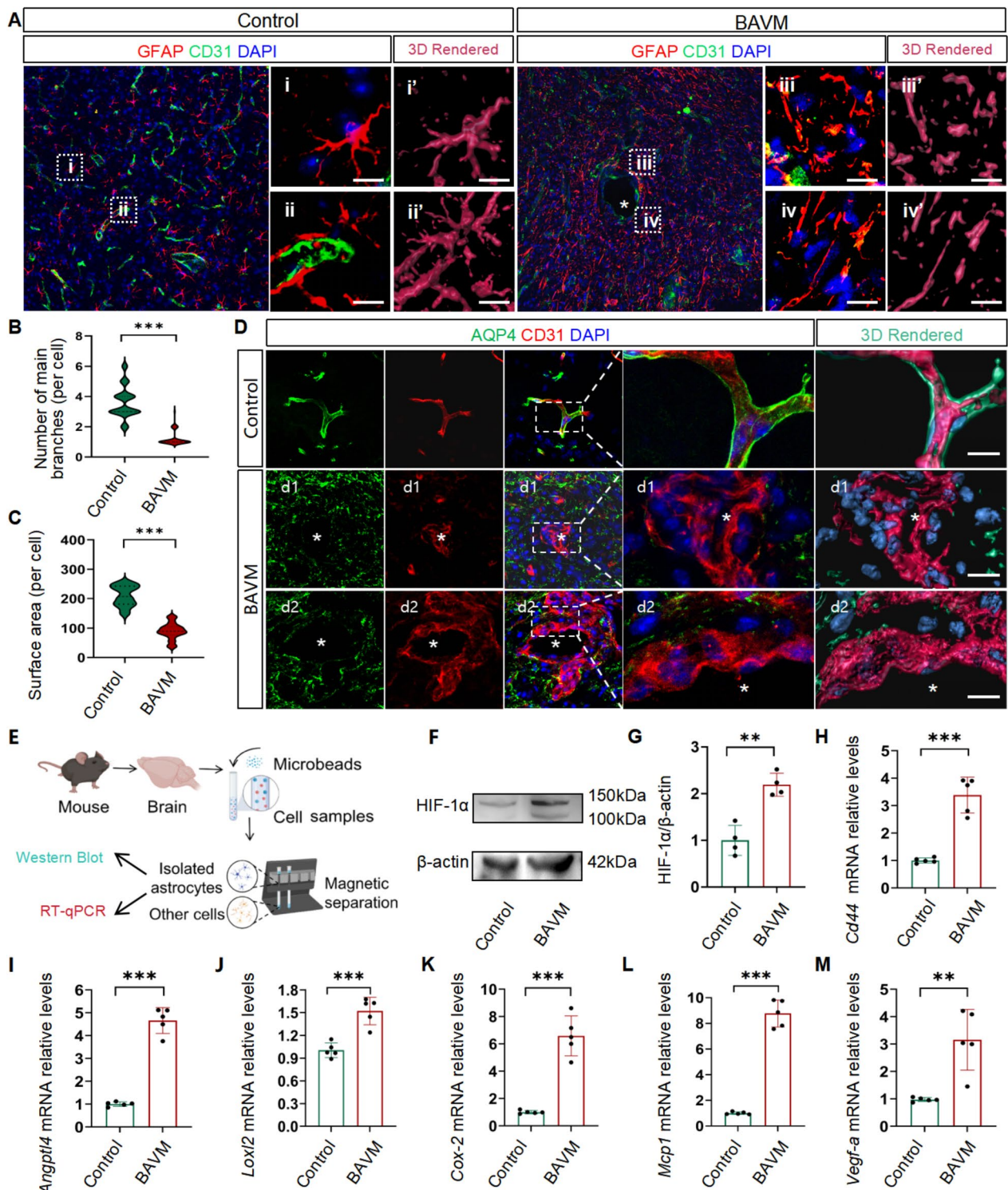


Fig. 3 Astrocytes in the BAVM pathological microenvironment exhibit unique phenotypic changes. **A** Representative fluorescence images of immunostaining with GFAP and CD31. Images of (i)–(iv) were locally magnified images. Images of (i′)–(iv′) were 3D-rendered images of immunostaining with GFAP. Scale bar = 10 μm. The asterisk (*) represents the vascular lumen of BAVM. **B, C** The quantification of astrocytes’ main branches number and surface area (n = 3 mice). **D** Representative fluorescence images of immunostaining with AQP4 and CD31. Scale bar = 10 μm. The asterisk (*) represents the vascular lumen of BAVM. **E** A schematic illustrating the extraction of primary astrocytes from fresh brain tissues. **F** Representative western blot images of HIF-1α of control and BAVM group. **G** The quantification of HIF-1α/β-actin (n = 4 mice). **H–M** Relative mRNA levels of *Cd44*, *Angptl4*, *Loxl2*, *Cox-2*, *Mcp1* and *Vegf-a* in astrocytes from control and BAVM mice (n = 5 mice)

a phenotypic shift toward endothelial-to-mesenchymal transition (EndMT) was observed (Additional file 4: Fig. S4H), which is one of the key pathological features of BAVM endothelial cells [37]. Taken together, these results preliminarily reveal the phenotypic transformation of astrocytes in response to inflammatory and hypoxic signals within the BAVM microenvironment, which may further exacerbate endothelial dysfunction.

To more comprehensively reveal the transcriptional changes in astrocytes, we performed RNA-seq using RNA extracted from primary astrocytes (Fig. 4A). Firstly, we identified 422 upregulated and 385 downregulated genes (FDR < 0.05) between astrocytes from control and BAVM mice (Fig. 4B). Then, genes demonstrating significant changes can be primarily categorized into three major groups: neuroinflammation, oxidative stress, and vascular wall stability (Fig. 4C). Genes associated with inflammation and immune response, including *Cxcl1*, *Cxcl10*, *Ccl2*, *Il6*, *Tlr2*, and *Stat3*, were notably upregulated in the BAVM group, indicating enhanced inflammatory signaling. Markers of macrophage activation, such as *Arg1*, *Cd68*, and *Cd40*, were also elevated, suggesting a pro-inflammatory environment. Consistent with our findings, *Hif-1 α* and its target genes, including *Ptgs2* (COX-2), *Cd44*, *Angptl4*, and *Loxl2*, which are involved in hypoxia response, angiogenesis and extracellular remodeling, were significantly upregulated in astrocytes within the BAVM group. Oxidative stress-related genes (*Hmox1*, *Gpx1*, *Gsr* and *Sod2*) and metabolic regulators (*Pkm2* and *Sdha*) showed increased expression, reflecting heightened oxidative stress and metabolic reprogramming. Genes involved in vascular repair and dynamics, including *Vegfa*, *Angptl4*, and *Serpine1*, were upregulated, alongside matrix metalloproteinases (*Mmp3*, *Mmp9*, *Mmp10*, *Mmp12* and *Mmp13*), which are implicated in extracellular matrix remodeling and vascular fragility. Conversely, tight junction-related genes (*Tjp3*, *Cldn5*, *Esam*, and *Cldn3*, *Ocln*) were downregulated, suggesting compromised vascular integrity. Moreover,

GO enrichment analysis revealed significant alterations in Biological Processes (BP), with notable enrichment in cytokine-cytokine receptor signaling, chemotaxis, and leukocyte migration, which suggest a heightened inflammatory response and increased recruitment of immune cells to the affected area (Fig. 4D). In the Cellular Components (CC) category, genes were enriched in secretory granules, hemoglobin complexes, and platelet alpha granules, pointing to changes in protein secretion, storage, and cellular trafficking, potentially reflecting an altered cellular state (Fig. 4D). The Molecular Functions (MF) analysis highlighted strong enrichment in cytokine receptor binding and chemokine receptor binding, indicating activation of signaling pathways that are critical for inflammation and intercellular communication (Fig. 4D). Consistent with this, the KEGG pathway diagram highlighted the critical role of cytokine-cytokine receptor interactions in the BAVM microenvironment, initiating signaling events that may affect endothelial cell behaviors such as migration, permeability, and vascular stability. These results also underscored the central role of inflammation, immune dysregulation, and cellular communication in driving disease progression, highlighting them as key pathological features of the disease [38–40] (Fig. 4E). Similarly, pathways such as *IL-17* and *TNF* were also enriched, suggesting the critical role of inflammation, immune dysregulation, and cellular communication in disease progression, positioning them as key pathological features. Upon receptor activation, *NF- κ B*, *MAPK*, and *C/EBP* pathways were activated, leading to the transcription of pro-inflammatory cytokines such as *IL-6*, *TNF- α* , and *IL-1 β* (Fig. 4E). Conclusively, these findings highlighted that astrocytes in the BAVM microenvironment undergo significant transcriptional reprogramming, contributing to inflammation, oxidative stress, vascular remodeling, and vascular barrier dysfunction.

(See figure on next page.)

Fig. 4 RNA-seq reveals key molecular signatures of primary astrocytes in the BAVM pathological microenvironment. **A** A schematic illustrating the extraction of primary astrocytes from fresh brain tissues (n = 3 mice/group). **B** Volcano plot of differential gene expression from RNA-Seq analysis. **C** Heatmap of differential gene expression from RNA-Seq analysis. The data could be divided into three sections: Inflammation and immunity (top), hypoxia and oxidative stress (middle), and vascular wall stability and repair (bottom). The heatmap showed the expression levels of selected genes across different conditions, with rows representing genes and columns representing samples. Color intensity reflects the expression level, with red indicating high expression and blue indicating low expression. The genes are clustered based on their expression patterns. **D** Gene Ontology (GO) analysis of differentially expressed genes, including Biological Processes (BP), Cellular Components (CC), and Molecular Functions (MF). The plot showed the top enriched GO terms for each category, with the x-axis representing the significance ($-\log_{10}(\text{p value})$) and the y-axis listing the GO terms. Color intensity indicates the level of enrichment, with darker colors representing higher significance. **E** KEGG pathway analysis of differentially expressed genes. The plot showed the top enriched pathways, with the x-axis representing the significance ($-\log_{10}(\text{p-value})$) and the y-axis listing the KEGG pathways

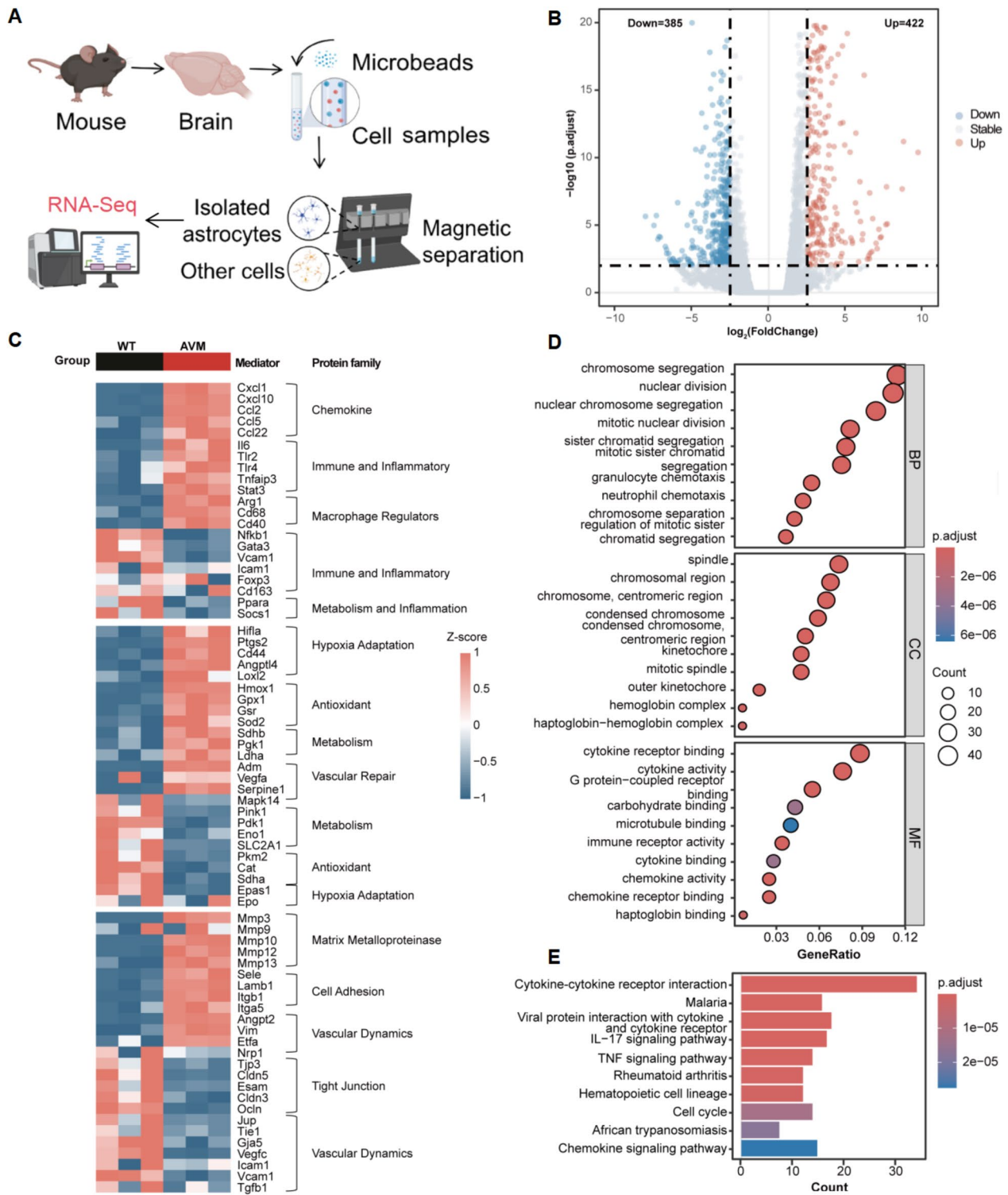


Fig. 4 (See legend on previous page.)

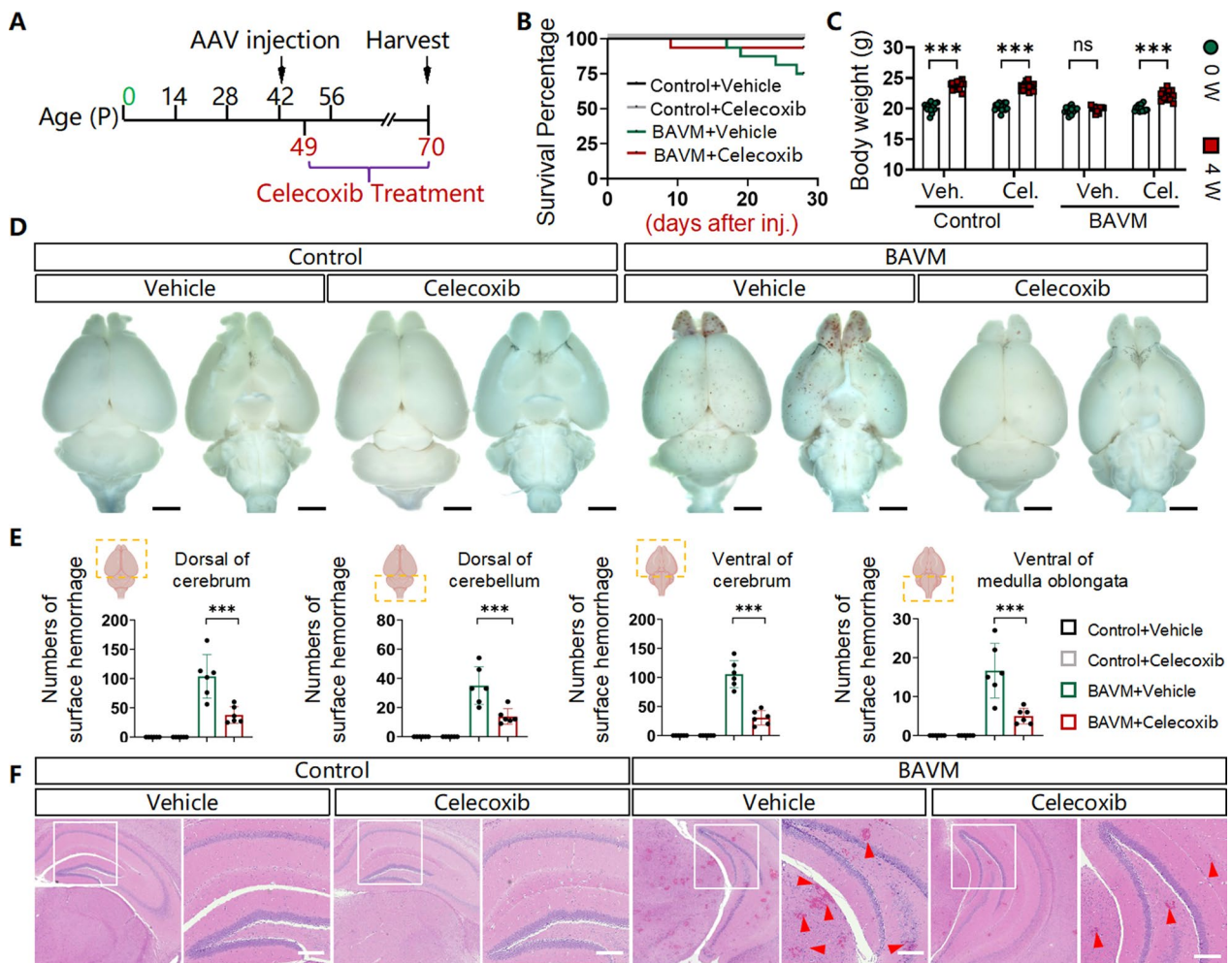


Fig. 5 COX-2 inhibition alleviates BAVM-related cerebral hemorrhage burden. **A** A diagram for the Celecoxib treatment protocol. **B** Survival curves of mice (n = 16 mice/group). **C** Body weight record of mice (n ≥ 10 mice/group). **D** Images of fresh brain tissue of each group. Scale bar = 2 mm. **E** The quantification of the number of surface hemorrhage (n = 6 mice). **F** Images of H&E staining of brain sections. Scale bar = 200 μm. Red arrows indicate hemorrhagic spots

COX-2 inhibition prevents BAVM-related hemorrhages in *Braf^{V600E}*-induced BAVM mice

Since we observed an increase in COX-2 at both the mRNA and protein levels in mouse BAVM lesion brain tissue, as well as at the mRNA level in BAVM astrocytes, a finding further supported by our RNA-seq results, we hypothesized that COX-2 may play a pivotal role in driving inflammation and pathological remodeling within the BAVM microenvironment. To explore this, we investigated the effects of Celecoxib, a nonsteroidal anti-inflammatory drug (NSAID) that specifically inhibits COX-2 activity, in this preclinical BAVM model. One week after AAV injection, we began administering Celecoxib (40 mg/kg). After three weeks

of administration, we collected samples for observation (Fig. 5A). In Fig. 5B, C, we can see that drug intervention dose not affect the survival rate or weight change in control mice. However, in the BAVM group, mice treated with Celecoxib showed normal weight gain. Next, blinded assessments revealed that the number of brain surface hemorrhages was reduced in Celecoxib-treated mice compared to vehicle-treated controls (Fig. 5D, E). H&E staining also revealed that COX-2 inhibition reduced the density of hemorrhagic foci in BAVM mice (Fig. 5F).

Hemorrhagic foci may lead to neuronal apoptosis, thereby affecting neurological function. We used TUNEL staining to reveal neuronal apoptosis surrounding the

lesions and found that neuronal apoptosis was significantly reduced in the BAVM mice treated with Celecoxib (Fig. 6A, B). Furthermore, we assessed the effect of COX-2 inhibition on neurological function in BAVM mice. In the following experiments, we conducted mouse behavioral assessments using the rotarod test, hanging wire test, and balance beam test. The results showed that Celecoxib intervention in BAVM mice significantly improved behavioral scores, indicating enhanced motor function, muscle strength, and balance (Fig. 6C–F). The mice's learning and memory abilities were assessed in the Morris water maze test by analyzing their movement trajectories in the circular maze (Fig. 6G–J). Compared to vehicle-treated BAVM mice, Celecoxib-treated BAVM mice exhibited a higher crossing frequency, spent more time approaching the platform during the testing phase, and showed a shorter escape latency, indicating the recovery of impaired neurological function. Additionally, we used the open field test to further assess the mice's motor and exploratory abilities (Fig. 6K, L). BAVM mice exhibited a preference for remaining in the corners of the box, in contrast to the normal exploratory behavior observed in healthy mice, which freely navigate the entire space. However, COX-2 inhibition restored these functions, with Celecoxib-treated BAVM mice covering a longer distance compared to the vehicle-treated BAVM mice. Overall, these data suggested that intracranial hemorrhage caused by BAVM may lead to neuronal apoptosis, impairing motor function, balance, and learning abilities. However, COX-2 inhibition significantly alleviated the hemorrhage and restored the impaired neurological functions.

COX-2 inhibition improves the hypoxic and neuroinflammatory microenvironment and reverses astrocyte pathology

The therapeutic effect of COX-2 inhibition in reducing hemorrhage is evident. In the following experiments, we further investigated the exact mechanism through which it exerts its effect. Firstly, immunofluorescence staining and Western blot analysis revealed a significant reduction in eNOS expression in the Celecoxib-treated BAVM mice compared to the vehicle-treated group (Fig. 7A–C). Meanwhile, RT-qPCR results showed a decrease in the

expression of *Nos3* and *Vegf-A* in the Celecoxib-treated BAVM mice (Fig. 7D, E). These changes suggested that Celecoxib treatment alleviated hypoxic and oxidative stress conditions in the pathological microenvironment of BAVM, which may be directly related to vascular wall remodeling. In support of this, the Evans Blue Dye perfusion experiment showed reduced leakage in the Celecoxib-treated BAVM mice compared to the vehicle-treated group (Fig. 7F, G). In line with this, the vascular coverage of tight junction proteins, including OCCLUDIN and CLAUDIN-5, was significantly restored after Celecoxib treatment (Fig. 7H–K). These data confirmed that the improvement in the pathological microenvironment is closely linked to enhanced vascular wall remodeling and stability. Meanwhile, the reduction in leakage and bleeding further alleviated hypoxia and neuroinflammation around the lesion. Ultimately, this treatment helped break the vicious cycle, promoting the restoration of microenvironmental homeostasis and vascular repair.

As a supplement, we explored the potential drug targets of Celecoxib in BAVM disease through pharmacological network analysis (The analysis process is presented in Additional file 5: Fig. S5). Gene data (drug target genes and disease-related genes) were extracted following the process shown in Additional file 6: Fig. S6. Among 491 drug target genes and 1709 BAVM-related genes, we identified 114 overlapping targets. Protein–protein interaction (PPI) analysis of the 114 overlapping genes was performed using STRING and Cytoscape (Additional file 6: Fig. S6 A). Then, we used Venn diagram to perform a cross-analysis of the top 20 key target genes ranked by three parameters (degree, closeness centrality and betweenness centrality), resulting in 14 key target genes of Celecoxib for treating BAVM (Additional file 6: Fig. S6B, C). Consistent with our findings, among the 14 key target genes, HIF-1 α , COX-2 (PTGS2), and MMP9 were identified, which undoubtedly strengthens the evidence supporting our research results (Additional file 6: Fig. S6D). Pathway enrichment analysis revealed that these key genes are involved in multiple critical signaling pathways, including those related to metabolism, hypoxia response, and normoxic stabilization (Additional file 6: Fig. S6E). These results provided evidence supporting the

(See figure on next page.)

Fig. 6 COX-2 inhibition reduces BAVM-associated neurological deficits. **A** Representative fluorescence images of immunostaining with TUNEL, NeuN and CD31. Images of (i')–(iv') were locally magnified images. Scale bar = 10 μ m. The asterisk (*) represents the vascular lumen of BAVM. **B** The quantification of the number of TUNEL positive neurons (n = 6 mice). **C–F** Scoring statistics of the Beam Balance test, Rotarod test, Wire Hang test, and rodent behavioral assessments (n = 6 mice). **G–J** Representative trajectory maps and statistical results of escape latency, platform crossovers and approaching platform time from the Morris Water Maze test (n = 6 mice). **K, L** Representative trajectory maps and statistical results from the Open Field test (n = 6 mice)

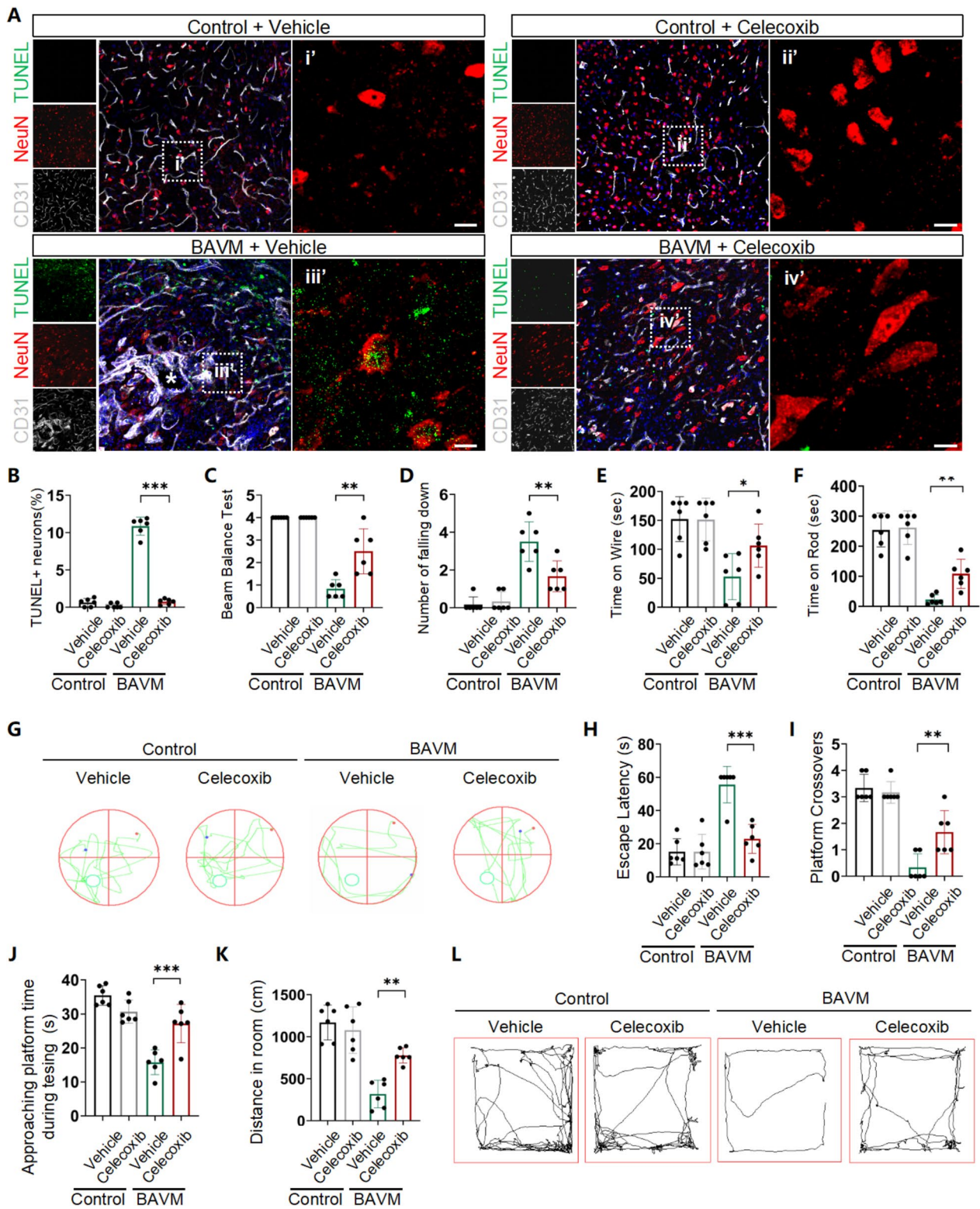


Fig. 6 (See legend on previous page.)

role of Celecoxib in regulating hypoxia-related and cellular stress responses.

Next, we evaluated the effect of COX-2 inhibition on astrocyte states. Our results showed that Celecoxib treatment significantly reduced HIF-1 α levels in BAVM-astrocytes (Fig. 8A, B). Furthermore, RT-qPCR analysis revealed that a significant reduction of HIF-1 α regulated genes, including *Mcp1* and *Vegf-a* in the Celecoxib-treated BAVM group when compared with vehicle-treated BAVM group (Fig. 8C, D). Additionally, in Fig. 8E, we observed that the distinct phenotype of astrocytes surrounding BAVM lesions reverted to a more normal state following Celecoxib treatment, with significant improvements in cell morphology, branching, and cell area compared to the vehicle treatment group (Fig. 8E, G, H). Similarly, we also assessed the coverage of astrocyte end-feet. As shown in Fig. 8F, I, after Celecoxib treatment, the coverage of astrocyte end-feet around the blood vessel walls was also restored. Collectively, these results suggested that the BAVM microenvironment may promote disease progression by inducing phenotypic changes in astrocytes (Fig. 8J). Furthermore, the ability of Celecoxib to rescue astrocyte phenotype also highlighted its therapeutic potential targeting the pathological microenvironment of BAVM.

Discussion

The propensity of BAVM lesions to form and rupture within the central nervous system parenchyma has not yet been mechanistically elucidated. Here, we proposed a non-endothelial mechanism in which Astrocytes respond to hypoxia and neuroinflammation in the BAVM pathological microenvironment, interacting with endothelial cells to exacerbate the pathological cascade. First, our study suggested that hypoxia and inflammation play a more critical role in the transition and progression of BAVM lesions. Moreover, through RNA sequencing analysis of primary astrocytes, we discovered that astrocytes within BAVM lesions acquire a reactive phenotype and neuroinflammatory capacity, contributing to leukocyte chemokine production, antigen presentation, and inflammatory responses. More

importantly, our study introduced the concept of the pathological microenvironment and astrocyte interaction driving a vicious cycle in the pathogenesis of BAVM. This insight highlighted the potential of targeting the microenvironment to disrupt this cycle, offering new therapeutic strategies for BAVM disease.

For years, the pathological microenvironment of BAVM has gradually garnered attention, where the pathological remodeling of the “neuro-glial-vascular” unit is initiated under the primary drive of genetic mutations in endothelial cells [41, 42]. Hemorrhagic or ischemic events trigger an endothelial “response-to-injury” paradigm, resulting in localized vascular dysregulation and angiogenesis imbalance [41]. Our previous work has depicted intense neuroinflammation in BAVM lesions, which may be a consequence of hemorrhage or another contributing factor that exacerbates vascular wall damage [20]. For example, the increased expression and activity of MMPs in a strong inflammatory microenvironment may be key factors affecting vascular remodeling, and interventions targeting this point could also have potential [43–45]. Our current research also revealed that the BAVM microenvironment is characterized by the abnormal expression of hypoxia and oxidative stress-related markers. In turn, oxidative stress may further contribute to endothelial dysfunction while affecting the function of other cells surrounding the lesion, such as astrocytes. Meanwhile, increased levels of eNOS protein and NO bioavailability are associated with elevated HIF-1 α and VEGF levels in astrocytes, as confirmed in CCM diseases [13, 46]. These findings were consistent with previous reports indicating that a basal level of endothelial NO plays a key role in maintaining homeostasis between the endothelium and surrounding parenchyma [29, 30].

Astrocytes, the most abundant glial cells in the central nervous system, aid in regulating blood flow and supporting vascular function through their interactions with endothelial cells [33, 34]. Our study revealed previously unknown links between distinct neuroinflammatory astrocytes and the BAVM microenvironment, identifying them as contributors

(See figure on next page.)

Fig. 7 COX-2 inhibition alleviates neuroinflammation and oxidative stress in the BAVM pathological microenvironment. **A** Representative fluorescence images of immunostaining with CD31 and eNOS. Scale bar = 20 μ m. The asterisk (*) represents the vascular lumen of BAVM. **B** Representative western blot images of eNOS in brain tissue. **C** The quantification of eNOS/ β -actin (n = 4 mice). **D, E** Relative mRNA levels of *Nos3* and *Vegf-a* in each group (n = 5). **F** The quantification of the Evans Blue Dye fluorescence area of each group (n = 6 mice). **G** Representative images of Evans Blue Dye perfusion. Scale bar = 20 μ m. The asterisk (*) represents the vascular lumen of BAVM. **H** Representative fluorescence images of immunostaining with CD31 and OCLN (OCLN) for each group. Scale bar = 20 μ m. The asterisk (*) represents the vascular lumen of BAVM. **I** The quantification of the ratio of OCLN + vessels/CD31 + vessels (%) (n = 6 mice). **J** Representative fluorescence images of immunostaining with CD31 and CLAUDIN-5 (CLDN5) for each group. Scale bar = 20 μ m. The asterisk (*) represents the vascular lumen of BAVM. **K** The quantification of the ratio of CLDN5 + vessels/CD31 + vessels (%) (n = 6 mice)

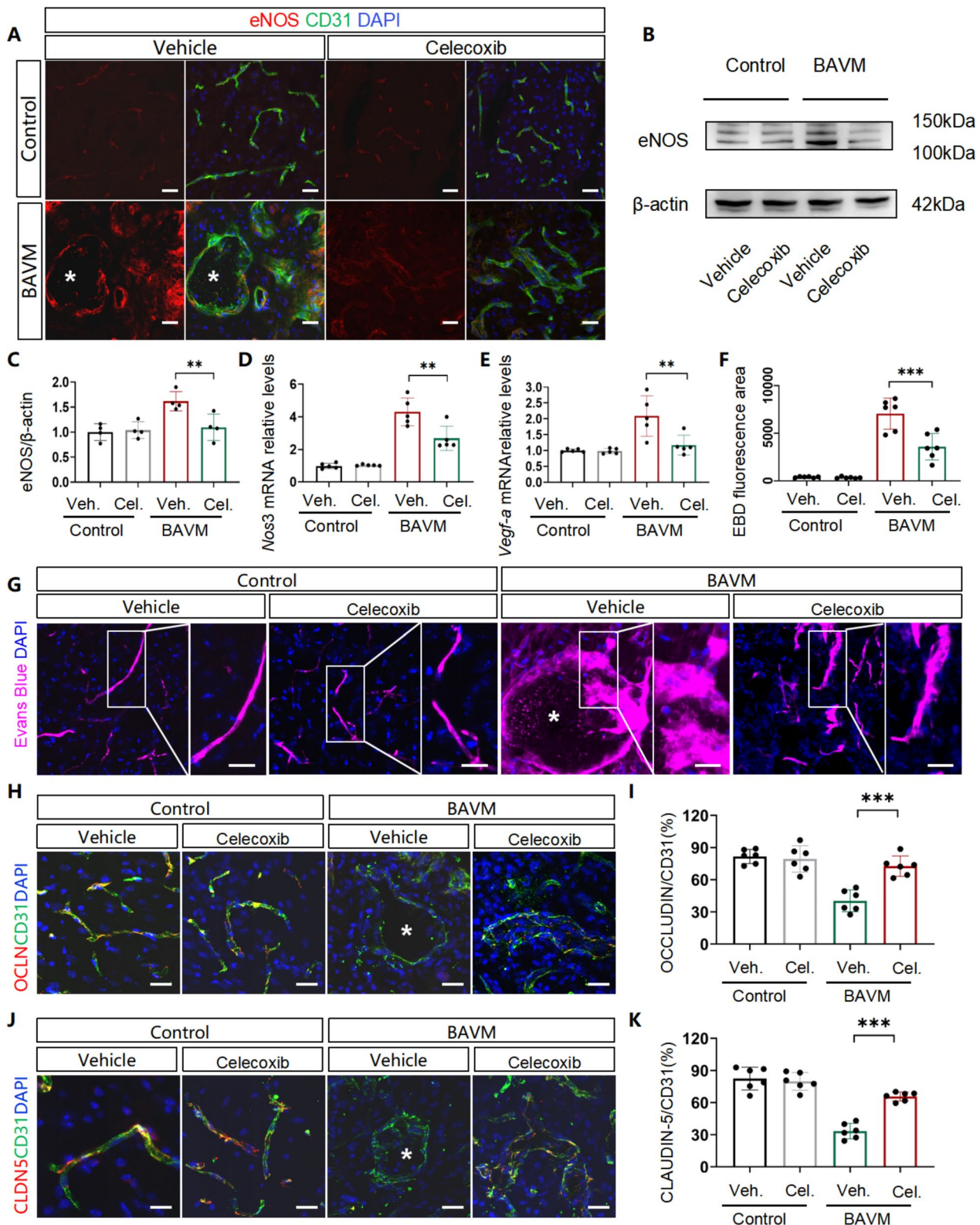


Fig. 7 (See legend on previous page.)

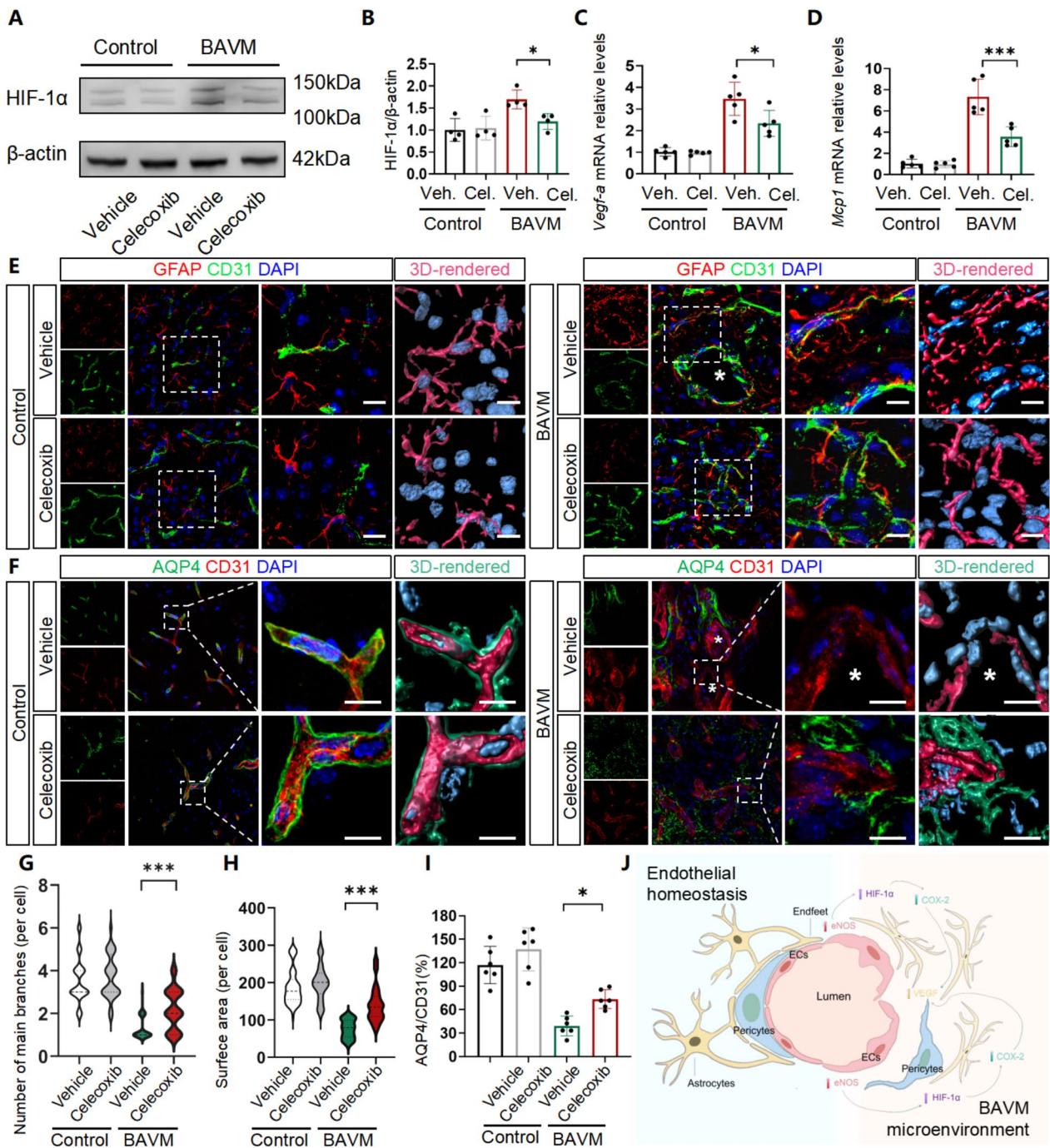


Fig. 8 COX-2 inhibition rescues astrocytes in the BAVM pathological microenvironment. **A** Representative western blot images of HIF-1α in brain tissue. **B** The quantification of HIF-1α/β-actin (n = 4 mice). **C, D** Relative mRNA levels of *Vegf-a* and *Mcp1* in each group (n = 5 mice). **E** Representative fluorescence images and 3D rendered images of immunostaining with GFAP and CD31. Scale bar = 10 μm. The asterisk (*) represents the vascular lumen of BAVM. **F** Representative fluorescence images and 3D rendered images of immunostaining with AQP4 and CD31. Scale bar = 10 μm. The asterisk (*) represents the vascular lumen of BAVM. **G, H** The quantification of astrocyte's main branch number and surface area for per cell (n = 30 cells from 6 mice). **I** The quantification of the ratio of AQP4 + vessels/CD31 + vessels (%) (n = 6 mice). **J** A diagram illustrating normal endothelial homeostasis and pathological microenvironment of BAVM

that trigger vascular remodeling. Previous studies have reported that reactive astrocytes under inflammatory conditions, such as ischemic or hemorrhagic stroke, exhibit varying degrees of polarization [12, 47]. This polarization is primarily characterized by distinct phenotypic shifts, including pro-inflammatory (A1) and anti-inflammatory or neuroprotective (A2) states, with differential expression of cytokines, growth factors, and metabolic markers. Interestingly, our study found that astrocytes around the BAVM lesions exhibit significant morphological changes, becoming more elongated with reduced branching. This phenomenon suggested that under hypoxic and inflammatory conditions, astrocytes may undergo a phenotypic shift resembling reactive gliosis or pathological astrocytic remodeling [48]. Such changes could indicate a loss of their supportive function and a shift toward exacerbating neurovascular dysfunction, potentially through enhanced inflammatory responses and extracellular matrix remodeling [7–10]. Our RNA-Seq results from primary astrocytes provided functional explanations for the observed phenotypic transition. First, the significant differential expression of inflammatory genes suggested that astrocytes in the BAVM environment may become activated, contributing to neuroinflammation, which could exacerbate endothelial dysfunction. Additionally, we confirmed the high reactivity of HIF-1 α in astrocytes under BAVM pathological conditions and the elevated levels of *Vegf-a*, leading to an increase in the production of pro-angiogenic and inflammatory factors, including *Cd44*, *Angptl4*, and *Loxl2*. These factors could induce vascular dysfunction by triggering inflammation and angiogenesis. HIF-1 α is a transcription factor that plays a key role in cellular adaptation to low-oxygen environments [13, 36]. When cells are exposed to hypoxia, HIF-1 α promotes the expression of various genes to help cells adapt to oxygen deprivation. Previous work by Nagore I. and colleagues identified the role of HIF-1 α in the progression of BAVM disease and emphasized the potential clinical value of targeting HIF-1 α for therapeutic interventions, which may reduce and potentially reverse AVMs [43]. Other researches have confirmed that the increased production of NO by brain endothelial cells stabilizes HIF-1 α in astrocytes, leading to elevated VEGF production and the activation of a “hypoxic” program under normoxic conditions [13]. Overall, our study found that these astrocytes undergo a series of changes in response to the pathological microenvironment of BAVM. In this context, these astrocytes contributed to the further destabilization of the vascular wall through hypoxic and inflammatory processes.

COX-2, an enzyme involved in prostaglandin biosynthesis during inflammation, is often upregulated under hypoxic conditions [16–19]. This upregulation has been reported to be typically induced by HIF-1 α , which acts as a transcription factor in response to low oxygen levels [13, 16]. As previous studies have demonstrated, COX-2 inhibition can suppress angiogenesis both in vivo and in vitro [49, 50], and thus we focused on COX-2 inhibition during the progression of BAVM to investigate its therapeutic potential for regulating angiogenesis and improving vascular stability in the pathological microenvironment of BAVM. Notably, selective COX-2 inhibitors are safe and well-tolerated drugs that can be repurposed for treating BAVM disease. Our findings indicated that COX-2 inhibition effectively reduced hemorrhage in the BAVM disease model. Moreover, our pharmacological network analysis provided detailed insights for exploring the therapeutic targets of Celecoxib in the treatment of AVM disease. Consistent with our study, the analysis predicted molecular networks primarily involving targets such as COX-2, HIF-1 α , and MMPs. Importantly, the disease-related genes used in our analysis were sourced from databases such as GeneCard, OMIM, and TTD, specifically focusing on human species genes. Therefore, these results undoubtedly enhance the potential for the clinical translation of COX-2 inhibition therapy. However, the specific dose–response effects and treatment duration of COX-2 inhibitors for BAVM treatment still require thorough investigation to ensure efficacy and minimize side effects. Interestingly, we observed that inhibiting COX-2 not only reduced the density of hemorrhagic lesions in BAVM but also reversed the phenotype of astrocytes. Although this uncontrolled association cannot be interpreted as causality, it suggests that the improvement in hemorrhagic events is linked to the status of astrocytes within the lesions.

Overall, our study first revealed the complex molecular reprogramming of astrocytes in the BAVM microenvironment. This transcriptional shift not only drove a robust inflammatory response and exacerbates oxidative stress, but also contributed to vascular instability and blood–brain barrier dysfunction. The reprogramming of astrocytes highlighted their key role in altering the pathological landscape of BAVM by enhancing immune cell recruitment, promoting extracellular matrix remodeling, and increasing vascular fragility. There were several limitations to our research. First, the effect of COX-2 inhibition on the volume of BAVM lesions remains unclear, despite the generally slower progression of BAVM observed in clinical practice. In fact, previous studies have raised the

question of whether pharmacological interventions can reverse advanced cerebrovascular lesions in humans, which may have persisted for decades and undergone extensive remodeling due to chronic responses to altered blood flow and inflammation. Our study primarily investigated the effects of microenvironment-targeted therapies on hemorrhage risk in BAVM. However, the potential for reversing the pathological architecture of BAVM following microenvironmental improvement remains an area for further investigation. This is also a desired outcome of research in this field, or at least, could serve as part of a combination therapy approach. Second, though our sequencing data preliminarily revealed transcriptional changes in astrocytes, the impact of these uniquely phenotyped astrocytes on endothelial cells and vasculature, as well as the precise mechanisms underlying this interaction, warrants comprehensive investigation. After all, the pathology of this disease predominantly involves endothelial cell dysfunction and vascular abnormalities.

Conclusion

In conclusion, our research shows that the interaction between the BAVM pathological microenvironment and astrocytes drives the progression and rupture of BAVM lesions, contributing to neurovascular dysfunction. This regulatory mechanism is intricately linked to HIF-1 α /COX-2, suggesting a novel perspective on the dysfunctional state of astrocytes in BAVM pathological microenvironment. Future therapeutic strategies targeting the microenvironment may serve as interventions to reduce the hemorrhage risk in BAVM patients.

Abbreviations

BAVM	Brain arteriovenous malformation
AAV	Adeno associated virus
NO	Nitric oxide
CNS	Central nervous system
COX-2	Cyclooxygenase-2
GFAP	Glial fibrillary acidic protein
PBS	Phosphate-buffered saline
PFA	Paraformaldehyde
H&E	Hematoxylin and eosin
GO	Gene ontologies
KEGG	Kyoto Encyclopedia of Genes and Genomes
DEGs	Differentially expressed gene
eNOS	Endothelial nitric oxide synthase
HIF1- α	Hypoxia-inducible factor-1 α
EBD	Evans Blue Dye
ECM	Extracellular matrix
Mcp1	Monocyte chemoattractant protein-1
BP	Biological processes
CC	Cellular components
MF	Molecular functions
NSAID	Nonsteroidal anti-inflammatory drug
TUNEL	Terminal deoxynucleotidyl transferase-mediated dUTP nick-end labeling
CCM	Cavernous malformation

Supplementary Information

The online version contains supplementary material available at <https://doi.org/10.1186/s12974-025-03442-2>.

Additional file 1: Fig. S1. High labeling efficiency and specificity of AAV-BR1-EGFP.A diagram illustrating the protocol for AAV injection and validation.Representative fluorescence images of immunostaining for EGFP and CD31 in the cerebrum, cerebellum, and medulla. Scale bar = 20 μ m.

Additional file 2: Fig. S2. Activation of the *Brat*^{600E} mutation drives the development and progression of BAVMs in mice.A diagram illustrating the model establishment and observation timeline.Survival curves of mice in each group.Images of fresh brain tissues in each group. Scale bar = 500 μ m.

Additional file 3: Fig. S3. In Vitro Experiments Reveal that Endothelial Cells from BAVM Can Induce Astrocyte Phenotypic Transformation.A diagram illustrating ECs from control and BAVM mice co-cultured with control astrocytes and reactive astrocytes respectively using Transwell. Representative fluorescence images of immunostaining with HIF-1 α and GFAP for control astrocytes and reactive astrocytes group. Scale bar = 20 μ m.Representative western blot images of HIF-1 α of each group.The quantification of HIF-1 α / β -actin.Relative mRNA levels of *Cox-2* and *Vegf-a* in control and BAVM ECs co-cultured with control astrocytes and reactive astrocytes respectively. As = Astrocyte.

Additional file 4: Fig. S4. In Vitro Experiments Reveal the Impact of Reactive Astrocytes on Endothelial Function.A diagram illustrating the extraction of conditioned medium from control astrocytes and reactive astrocytes respectively, for interference with ECs.Relative mRNA levels of *Icam-1* and *Vcam-1* in CA-CM + EC group and RA-CM + EC group.Representative western blot images of OCCLUDIN.The quantification of OCCLUDIN/ β -actin.Representative western blot images of ZO-1.The quantification of ZO-1/ β -actin.Representative fluorescence images of immunostaining EndMT markers and CD31 for CA-CM + EC group and RA-CM + EC group. Scale bar = 20 μ m. CA = Control Astrocyte; RA = Reactive Astrocyte; CM = Conditioned medium; CA-CM = Conditioned medium of Control Astrocytes; RA-CM = Conditioned medium of Reactive Astrocytes.

Additional file 5: Fig. S5. Workflow of pharmacological network analysis. Targets of Celecoxib were identified utilizing Pharmmapper, Swiss Target Prediction and Super-PRED database. Genes associated with BAVM were obtained from GeneCards, OMIM and TTD database.

Additional file 6: Fig. S6. Pharmacological network analysis reveals therapeutic targets of Celecoxib.Venn diagram of Celecoxib-BAVM overlapping targets.PPI network of Celecoxib-BAVM intersection targets.Venn diagram of degree/BC/CC overlapping key targets.Key targets of Celecoxib for treating BAVM.KEGG pathways enrichment analysis.

Additional file 7: Fig. S7. Raw images of western blot.

Acknowledgements

I sincerely thank Dr. Yongjie Ma for generously providing me with a laptop to support my MD studies, including research and manuscript writing.

Author contributions

Tianqi Tu, Zhenghong Peng and Yong Jiang conceptualized the study and designed experiments; Tianqi Tu conducted the majority of experiments with help from Zhenghong Peng, Lihan Zhang, Jieru Yang, Kecheng Guo, Xiaogang Tang, Jiasen Ye, Fan Zhang and An Huang; Jianhua Peng, Donghai Wang, Jiaxing Yu, Changren Huang and Hongqi Zhang provided professional guidance and advice during the research process; all authors acquired data; Tianqi Tu, Zhenghong Peng and Lihan Zhang analysed the data; Tianqi Tu wrote the original draft of the manuscript; Jianhua Peng, Donghai Wang and Yong Jiang revised and corrected the manuscript. Tianqi Tu secured funding; all authors edited and approved the manuscript.

Funding

This work was supported by grants from the National Natural Science Foundation of China (U24 A20689, 82371310, 82271306), the Sichuan Science and Technology Program (No. 2024 NSFSC2098) and Research Start-up Fund

of the Affiliated Hospital of Southwest Medical University (No. 24082, No. 24083).

Data availability

No datasets were generated or analysed during the current study.

Declarations

Ethics approval

All animal procedures were conducted in accordance with the National Institutes of Health guidelines for the Care and Use of Laboratory Animals and were approved by the Animal Committee of the Ethics Committee of Southwest Medical University (Approval Number: 20220223-010).

Competing interests

The authors declare no competing interests.

Author details

¹Department of Neurosurgery, The Affiliated Hospital Southwest Medical University, No. 25 of Taiping Street, Luzhou 646000, Sichuan, China. ²Laboratory of Neurological Diseases and Brain Function, the Affiliated Hospital, Southwest Medical University, Luzhou, China. ³Sichuan Clinical Research Center for Neurosurgery, The Affiliated Hospital, Southwest Medical University, Luzhou, China. ⁴Institute of Brain Science, Southwest Medical University, Luzhou, China. ⁵Department of Neurosurgery, Xuanwu Hospital, China International Neuroscience Institute, Capital Medical University, Beijing, China. ⁶Medical Integration and Practice Center, Shandong University, Jinan, Shandong, China. ⁷Department of Neurosurgery and Shandong Key Laboratory of Brain Health and Function Remodeling, Qilu Hospital of Shandong University, Jinan 250000, Shandong, China. ⁸Department of Neurosurgery, Qilu Hospital of Shandong University Dezhou Hospital (Dezhou, China), Cheeloo Hospital of Shandong University, Jinan, Shandong, China.

Received: 31 January 2025 Accepted: 11 April 2025

Published online: 29 April 2025

References

- Solomon RA, Connolly ES Jr. Arteriovenous malformations of the brain. *N Engl J Med*. 2017;376:1859–66.
- Stapf C, Labovitz DL, Sciacca RR, et al. Incidence of adult brain arteriovenous malformation hemorrhage in a prospective population-based stroke survey. *Cerebrovasc Dis*. 2002;13:43–6.
- van Beijnum J, van der Worp HB, Buis DR, et al. Treatment of brain arteriovenous malformations: a systematic review and meta-analysis. *JAMA*. 2011;306:2011–9.
- Mohr JP, Overbey JR, Hartmann A, et al. Medical management with interventional therapy versus medical management alone for unruptured brain arteriovenous malformations (ARUBA): final follow-up of a multicentre, non-blinded, randomised controlled trial. *Lancet Neurol*. 2020;19:573–81.
- Hauer AJ, Kleinloog R, Giuliani F, et al. RNA-sequencing highlights inflammation and impaired integrity of the vascular wall in brain arteriovenous malformations. *Stroke*. 2020;51:268–74.
- Nielsen CM, Zhang X, Raygor K, et al. Endothelial Rbpj deletion normalizes Notch4-induced brain arteriovenous malformation in mice. *J Exp Med*. 2023;220:e20211390.
- Koehler RC, Roman RJ, Harder DR. Astrocytes and the regulation of cerebral blood flow. *Trends Neurosci*. 2009;32:160–9.
- Cohen-Salmon M, Slaoui L, Mazare N, et al. Astrocytes in the regulation of cerebrovascular functions. *Glia*. 2021;69:817–41.
- Baldwin KT. Molecular diversity of astrocytes. *Science*. 2022;378:475–6.
- Lee HG, Wheeler MA, Quintana FJ. Function and therapeutic value of astrocytes in neurological diseases. *Nat Rev Drug Discov*. 2022;21:339–58.
- Lee HG, Rone JM, Li Z, et al. Disease-associated astrocyte epigenetic memory promotes CNS pathology. *Nature*. 2024;627:865–72.
- Zhang F, Zhou J, Lu P, et al. Lactylation of histone by BRD4 regulates astrocyte polarization after experimental subarachnoid hemorrhage. *J Neuroinflammation*. 2024;21:186.
- Lopez-Ramirez MA, Lai CC, Soliman SI, et al. Astrocytes propel neurovascular dysfunction during cerebral cavernous malformation lesion formation. *J Clin Invest*. 2021;131:e139570.
- Lai CC, Nelsen B, Frias-Anaya E, et al. Neuroinflammation plays a critical role in cerebral cavernous malformation disease. *Circ Res*. 2022;131:909–25.
- Ge J, Zhou Y, Li H, et al. Prostacyclin synthase deficiency leads to exacerbation or occurrence of endothelium-dependent contraction and causes cardiovascular disorders mainly via the non-TxA(2) prostanoids/TP axis. *Circ Res*. 2024;135:e133–49.
- Kaidi A, Qualtrough D, Williams AC, et al. Direct transcriptional up-regulation of cyclooxygenase-2 by hypoxia-inducible factor (HIF)-1 promotes colorectal tumor cell survival and enhances HIF-1 transcriptional activity during hypoxia. *Cancer Res*. 2006;66:6683–91.
- Smith WL, DeWitt DL, Garavito RM. Cyclooxygenases: structural, cellular, and molecular biology. *Annu Rev Biochem*. 2000;69:145–82.
- Hasan D, Hashimoto T, Kung D, et al. Upregulation of cyclooxygenase-2 (COX-2) and microsomal prostaglandin E2 synthase-1 (mPGES-1) in wall of ruptured human cerebral aneurysms: preliminary results. *Stroke*. 2012;43:1964–7.
- Rodemer J, Junker A, Chen B, et al. Pathophysiology of intracranial aneurysms: COX-2 expression, iron deposition in aneurysm wall, and correlation with magnetic resonance imaging. *Stroke*. 2020;51:2505–13.
- Hong T, Yan Y, Li J, et al. High prevalence of KRAS/BRAF somatic mutations in brain and spinal cord arteriovenous malformations. *Brain*. 2019;142:23–34.
- Tu T, Yu J, Jiang C, et al. Somatic Braf(V600E) mutation in the cerebral endothelium induces brain arteriovenous malformations. *Angiogenesis*. 2024;27:441–60.
- Ye Q, Jo J, Wang CY, et al. Astrocytic Slc4a4 regulates blood-brain barrier integrity in healthy and stroke brains via a CCL2-CCR2 pathway and NO dysregulation. *Cell Rep*. 2024;43(5):114193.
- Feng S, Wu C, Zou P, et al. High-intensity interval training ameliorates Alzheimer's disease-like pathology by regulating astrocyte phenotype-associated AQP4 polarization. *Theranostics*. 2023;13(10):3434–50.
- Gotkiewicz M, Capra J, Miettinen PO, Natunen T, Tanila H. Three-dimensional view of microglia-amyloid plaque interactions. *Glia*. 2025;73(1):196–209.
- Liu D, Liao P, Li H, et al. Regulation of blood-brain barrier integrity by Dmp1-expressing astrocytes through mitochondrial transfer. *Sci Adv*. 2024;10(26):eadk2913.
- Peng J, Pang J, Huang L, et al. LRP1 activation attenuates white matter injury by modulating microglial polarization through Shc1/PI3K/Akt pathway after subarachnoid hemorrhage in rats. *Redox Biol*. 2019;21:101121.
- Park ES, Kim S, Huang S, et al. Selective endothelial hyperactivation of oncogenic KRAS induces brain arteriovenous malformations in mice. *Ann Neurol*. 2021;89:926–41.
- Chen CA, Wang TY, Varadharaj S, et al. S-glutathionylation uncouples eNOS and regulates its cellular and vascular function. *Nature*. 2010;468:1115–8.
- Huang L, Cheng F, Zhang X, et al. Nitric oxide synthase and reduced arterial tone contribute to arteriovenous malformation. *Sci Adv*. 2023;9:eade7280.
- Jozkovicz A, Cooke JP, Guevara I, et al. Genetic augmentation of nitric oxide synthase increases the vascular generation of VEGF. *Cardiovasc Res*. 2001;51:773–83.
- Zhang R, Wang L, Zhang L, et al. Nitric oxide enhances angiogenesis via the synthesis of vascular endothelial growth factor and cGMP after stroke in the rat. *Circ Res*. 2003;92:308–13.
- Nikolaev SI, Vetiska S, Bonilla X, et al. Somatic activating KRAS mutations in arteriovenous malformations of the brain. *N Engl J Med*. 2018;378:250–61.
- Diaz-Castro B, Robel S, Mishra A. Astrocyte endfeet in brain function and pathology: open questions. *Annu Rev Neurosci*. 2023;46:101–21.
- Quintana FJ. Astrocytes to the rescue! Glia limitans astrocytic endfeet control CNS inflammation. *J Clin Invest*. 2017;127:2897–9.

35. Haj-Yasein NN, Vindedal GF, Eilert-Olsen M, et al. Glial-conditional deletion of aquaporin-4 (Aqp4) reduces blood-brain water uptake and confers barrier function on perivascular astrocyte endfeet. *Proc Natl Acad Sci U S A*. 2011;108:17815–20.
36. Majmundar AJ, Wong WJ, Simon MC. Hypoxia-inducible factors and the response to hypoxic stress. *Mol Cell*. 2010;40:294–309.
37. Li H, Nam Y, Huo R, et al. De novo germline and somatic variants convergently promote endothelial-to-mesenchymal transition in simplex brain arteriovenous malformation. *Circ Res*. 2021;129(9):825–39.
38. Frias-Anaya E, Gallego-Gutierrez H, Gongol B, et al. Mild hypoxia accelerates cerebral cavernous malformation disease through CX3CR1-CX3CL1 signaling. *Arterioscler Thromb Vasc Biol*. 2024;44:1246–64.
39. Joy MT, Ben Assayag E, Shabashov-Stone D, et al. CCR5 is a therapeutic target for recovery after stroke and traumatic brain injury. *Cell*. 2019;176:1143–57.
40. Semple BD, Frugier T, Morganti-Kossmann MC. CCL2 modulates cytokine production in cultured mouse astrocytes. *J Neuroinflammation*. 2010;7:67.
41. Rustenhoven J, Tanumihardja C, Kipnis J. Cerebrovascular anomalies: perspectives from immunology and cerebrospinal fluid flow. *Circ Res*. 2021;129:174–94.
42. Seebauer CT, Wiens B, Hintschich CA, et al. Targeting the microenvironment in the treatment of arteriovenous malformations. *Angiogenesis*. 2024;27:91–103.
43. Marin-Ramos NI, Thein TZ, Ghaghada KB, et al. miR-18a inhibits BMP4 and HIF-1 α normalizing brain arteriovenous malformations. *Circ Res*. 2020;127:e210–31.
44. Sun Z, Kemp SS, Lin PK, et al. Endothelial k-RasV12 expression induces capillary deficiency attributable to marked tube network expansion coupled to reduced pericytes and basement membranes. *Arterioscler Thromb Vasc Biol*. 2022;42:205–22.
45. Hashimoto T, Wen G, Lawton MT, et al. Abnormal expression of matrix metalloproteinases and tissue inhibitors of metalloproteinases in brain arteriovenous malformations. *Stroke*. 2003;34:925–31.
46. Cuttano R, Rudini N, Bravi L, et al. KLF4 is a key determinant in the development and progression of cerebral cavernous malformations. *EMBO Mol Med*. 2016;8:6–24.
47. Wang C, Li L. The critical role of KLF4 in regulating the activation of A1/A2 reactive astrocytes following ischemic stroke. *J Neuroinflammation*. 2023;20:44.
48. Conforti P, Mezey S, Nath S, et al. Fibrinogen regulates lesion border-forming reactive astrocyte properties after vascular damage. *Glia*. 2022;70:1251–66.
49. Flemming KD, Kumar S, Brown RD, et al. Predictors of initial presentation with hemorrhage in patients with cavernous malformations. *World Neurosurg*. 2020;133:e767–73.
50. Gately S, Li WW. Multiple roles of COX-2 in tumor angiogenesis: a target for antiangiogenic therapy. *Semin Oncol*. 2004;31:2–11.

Publisher's Note

Springer Nature remains neutral with regard to jurisdictional claims in published maps and institutional affiliations.